ELSEVIER

International Journal of Mass Spectrometry 188 (1999) 147–153

International Journal of Mass Spectrometry

Cross section for the production of N_2^+ ($X^2\Sigma_g^+$) ions by electron impact on N_2

N. Abramzon[a,b], R.B. Siegel[a,1], K. Becker[b,*]

[a]*Department of Physics, City College of CUNY, New York, NY 10031, USA*
[b]*Department of Physics and Engineering Physics, Stevens Institute of Technology, Hoboken, NJ 07030, USA*

Received 30 November 1998; accepted 15 January 1999

Abstract

A combination of electron scattering and laser-induced fluorescence (LIF) techniques has been employed in the direct experimental determination of the N_2^+ ($X\ ^2\Sigma_g^+$) ionization cross section as a function of electron energy from threshold to 200 eV. Electron impact on N_2 produces N_2^+ ground-state ions that are detected by pumping the $X\ ^2\Sigma_g^+ \rightarrow B\ ^2\Sigma_u^+$ (0,0) vibrational transition at 391 nm with a tunable dye laser and detecting the subsequent LIF of the $B\ ^2\Sigma_u^+ \rightarrow X\ ^2\Sigma_g^+$ (0,1) vibrational transition at 428 nm. LIF spectra obtained at different electron energies yield the relative $N_2^+(X)$ cross section which is put on an absolute scale by normalization to the absolute cross section value of Doering and Yang [J. Geophys. Res. 102 (1996) 9683] obtained from electron–electron coincidence ($e,2e$) experiments at 100 eV. (Int J Mass Spectrom 188 (1999) 147–153) © 1999 Elsevier Science B.V.

Keywords: Electron-impact ionization; Cross sections; Laser-induced fluorescence

1. Introduction

Electron-impact ionization cross sections of molecules are important quantities in a variety of applications as diverse as low-temperature processing plasmas, fusion edge plasmas, gas discharges, planetary, stellar, and cometary atmospheres, aeronomy, radiation chemistry, mass spectrometry, and chemical analysis [1,2]. Much effort has been devoted to the measurement of molecular ionization cross sections over the past 60 years as summarized in several recent reviews [1,3,4]. On the theoretical side, rigorous quantum mechanical calculations of ionization cross sections for molecular targets are beyond the capability of current quantum-mechanical electron collision theory for essentially all molecules [5,6]. As a consequence, simplistic additivity rules [7–11], semiempirical and semiclassical approaches [12–17], and the more rigorous Binary–Encounter Bethe (BEB) theory of Kim and collaborators [18–20] are frequently used to calculate molecular ionization cross sections.

For almost all molecules, the electron-impact ionization of the target resulting in the formation of the parent ion is dominated by processes leading to parent ion in the electronic ground state [1–3]. Electronically excited parent ions typically account for less than 10% of the total parent ionization cross section [1–3]. Two notable exceptions are molecular nitrogen (N_2)

* Corresponding author. E-mail: kbecker@stevens-tech.edu
[1] Present address: National Institute of Standards and Technology (NIST), Gaithersburg, MD 20899.

PII S1387-3806(99)00018-4

and oxygen (O_2) where there is a significant probability that electron impact ionization produces electronically excited parent N_2^+ and O_2^+ ions [21–24]. N_2 is perhaps the most thoroughly studied molecule in terms of its interactions with electrons both theoretically and experimentally [25]. There are three electronic states of N_2^+ which are appreciably populated following electron impact ionization of ground state N_2, the $X\ ^2\Sigma_g^+$ ground state and the $A\ ^2\Pi_u$ and $B\ ^2\Sigma_u^+$ excited states. The cross section for the ionization-excitation of the N_2^+ B state is rather well-known from various experiments (see [22] for a summary) as are the total N_2 ionization cross section [26] and the total N_2^+ parent ionization cross section [27–30]. On the other hand, the experimentally determined cross section of N_2^+ ions in the A state is known only to within an error margin of about 50% which can be attributed to the long radiative lifetime of the state [31,32,39]. This renders it impossible to estimate the cross section for the formation of N_2^+ ($X\ ^2\Sigma_g^+$) ground-state ions from other available ionization cross sections with reasonable confidence. We note that a direct experimental determination of the $N_2^+(X\ ^2\Sigma_g^+)$ cross section is difficult (see e.g. [25]). Recently, Doering and co-workers used the electron–electron coincidence $(e,2e)$ technique to study electron impact ionization–excitation processes in N_2 and O_2 [22–24] and obtained the branching ratios to the various final states of the resulting ions. In the case of N_2, their results, when combined with the known total parent N_2^+ ionization cross section, allowed the extraction of absolute cross sections for the formation of N_2^+ (X), $N_2^+(A)$, and $N_2^+(B)$ ions at 100 eV. Their cross sections of 86.9×10^{-18} cm^2 (X state), 87.9×10^{-18} cm^2 (A state), and 19.2×10^{-18} cm^2 (B state) with quoted error margins of less than 10% [23] agree well with the cross sections (at 100 eV) reported by Van Zyl and Pendleton [21]. Therefore, the cross section for the formation of N_2^+ ($X\ ^2\Sigma_g^+$) ions by electron impact on N_2 at 100 eV can now be considered a benchmark cross section. Unfortunately, both Doering and Yang [23] and Van Zyl and Pendleton [21] reported only a single cross section value at 100 eV.

We report the result of a direct experimental determination of the relative N_2^+ ($X\ ^2\Sigma_g^+$) ionization cross section as a function of electron energy using a combination of electron scattering and laser-induced fluorescence (LIF) techniques. Electron impact on N_2 produces $N_2^+(X)$ ground-state ions which are detected by pumping the N_2^+ $X\ ^2\Sigma_g^+ \rightarrow B\ ^2\Sigma_u^+$ (0,0) vibrational transition at 391 nm with a tunable dye laser and detecting the subsequent fluorescence from the $B\ ^2\Sigma_u^+ \rightarrow X\ ^2\Sigma_g^+$ (0,1) vibrational transition at 428 nm. LIF spectra obtained at different electron energies yielded the relative $N_2^+(X)$ cross section which was put on an absolute scale by normalization to the absolute cross section value of Doering and Yang [23] at 100 eV. We note that a similar LIF technique was used previously by McConkey and co-workers [33] to study the rotational distribution of the $N_2^+(X)$ ions produced by electron impact ionization of N_2.

2. Experimental details

The experimental arrangement consists of a crossed electron-beam–gas-beam setup inside a stainless steel high-vacuum chamber which is pumped by a turbomolecular pump to a base pressure of 1×10^{-7} Torr. The two beams intersect at right angles. In addition, a tunable laser beam propagates either parallel or antiparallel to the electron beam in order to maximize the overlap of the three beams. Optical detection of the fluorescence from the interaction region is made perpendicular to both the electron beam and the gas beam. A schematic overview of the various components of the experimental apparatus is shown in Fig. 1.

The electron beam is produced by a modified Comstock electron monochromator which consists of a heated tungsten filament, a three-element electron gun, a 160° electric sector-field energy analyzer, and a three-element Einzel lens to focus the electron beam into the interaction region. The basic operation of the electron monochromator has been described in an earlier publication [34]. In the present application, where high energy resolution is not a crucial requirement, we operate the energy analyzer at a high

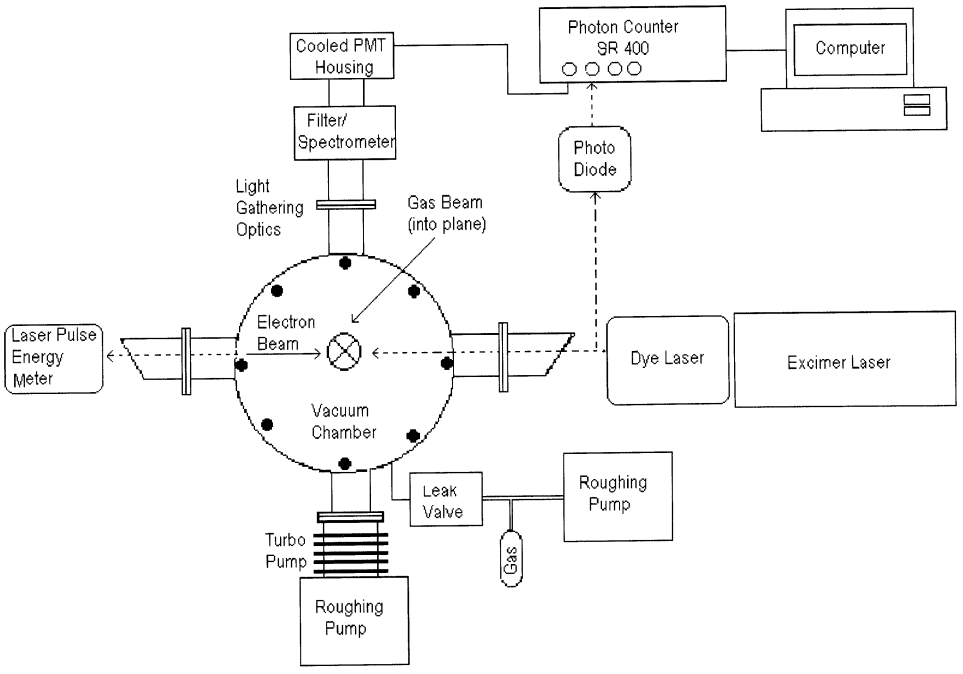

Fig. 1. Block diagram of the experimental arrangement. A top view of the vacuum chamber is given. Note that the electron beam and laser beam are propagating parallel or antiparallel and are oriented perpendicular to the gas beam which goes into the plane of the diagram. Also, the turbomolecular pumping station, which is mounted underneath the vacuum chamber, has been rotated by 90° in the diagram for ease of illustration.

transmission energy (50 eV or more), so that it acts merely as a bender for the electron beam. In addition, a 3 mm hole was drilled in the outer sector of the energy analyzer that allows passage of the laser beam in order to facilitate operation of the experiment with electron beam and laser beam propagating parallel or antiparallel through the interaction region. The energy resolution of the electron beam of about 0.5–0.7 eV [full width at half maximum (FWHM)] is essentially determined by the thermal energy spread of the electrons emitted from the heated tungsten filament. Beam currents in the interaction region of typically 5 μA at 25 eV and 20 μA at 100 eV could be achieved with a beam diameter of 2–3 mm. The electron beam can be operated continuously or pulsed with fall times of 10 ns or less. When the electron beam is operated continuously, the observed LIF signal is superimposed on a background from the continuous emission of the N_2^+ $B\ ^2\Sigma_u^+ \rightarrow X\ ^2\Sigma_g^+$ fluorescence resulting from the electron-impact ionization-excitation of N_2. Pulsing the electron beam eliminates this continuous background and improves the signal-to-noise ratio in the LIF spectrum. A pulsed electron beam, on the other hand, complicates the timing sequence of the data acquisition procedure.

The electron beam after traversing the interaction region is collected in a Faraday cup which consists of three electrically insulated elements. This enables us to measure the beam current as well as the beam divergence. The two outer elements of the Faraday cup are two concentric cylinders, one mounted inside the other and each having a 5 mm hole in the back to allow passage of the laser beam through the Faraday cup. In addition, a rectangular collector plate is mounted off-axis and parallel to the electron beam direction inside the second cup. The outer cylinder is kept at ground potential; the inner two elements are slightly positively biased, the inner cylinder at about +9 V and the collector plate at about +45 V. Thus the laser beam can exit or enter the Faraday cup unob-

structed, and the electron beam is collected by the various elements of the Faraday cup. The electron beam system is mounted on a circular stage attached to the top flange of the vacuum chamber which allows a fine height adjustment of the electron beam relative to the laser beam.

The gas beam is an effusive beam emanating from a multicapillary array of rectangular shape (11 mm in the direction parallel to the electron beam by 6 mm perpendicular to it), which is positioned about 8 mm above the electron beam axis. Modeling of the gas flow [35] using the model of Giordmane and Wang [36] demonstrated that about 50% of the total gas throughput passes through a rectangle of 11 mm by 6 mm (which corresponds to the size of the multicapillary array) in the interaction region. The pushing pressure behind the multicapillary nozzle is continuously monitored by a capacitance manometer. Pushing pressures up to 2 Torr are used under normal operating conditions resulting in estimated number densities of up to 3×10^{13} molecules/cm^3 in the interaction region.

The laser system consists of a pulsed Lumonics EX-520 excimer laser operating at 308 nm (XeCl). The excimer laser pumps a Lumonics HD-500 dye laser using Exalite 392A as the dye of choice in the wavelength region of the $X\ ^2\Sigma_g^+ \rightarrow B\ ^2\Sigma_u^+$ ($v' = 0$, $v'' = 0$) transition. The excimer laser produces 8–10 ns pulses of up to 100 mJ energy per pulse at a repetition rate of up to 100 Hz. The dye laser produces 0.0015-nm-wide pulses of up to 3 mJ energy per pulse in the wavelength range from 375 to 397 nm. The maximum laser pulse energy in the interaction is limited to about 300 μJ, which is well below the 450 μJ per pulse needed to saturate this particular N_2^+ transition [37]. The dye laser is equipped with a computer-controlled wavelength scan unit which allowed us to scan the output wavelength at very high resolutions (20 steps per unit line width). The laser beam enters and exists the vacuum chamber through Brewster-angle windows. The laser beam intensity passing through the vacuum chamber is monitored by a laser pulse energy meter.

The fluorescence from the interaction region is imaged onto the cathode of a thermoelectrically cooled Hamamatsu R1104 photomultiplier tube (PMT) by a system of two lenses and two variable apertures. Spectral isolation is achieved either by a narrow-band interference filter or by a compact low-resolution, high-throughput monochromator. Great care was exercised to minimize the amount of scattered laser light reaching the PMT by coating all elements inside the vacuum chamber in the path of the laser beam with Aerodag-G. In addition, light baffles were placed along the path of the laser beam and along the optical detection system. The two variable apertures allow us to control the interaction volume viewed by the PMT and help reduce the scattered laser light even further. The output pulses of the PMT are fed into a gated photon counter which has two gates of variable width (5–1000 ns) which can be scanned in variable increments of 5–1000 ns. The output of the gated photon counter, in turn, is directed into a personal computer for data storage and analysis.

3. Experimental procedure and data acquisition

All experimental parameters were optimized to (1) minimize scattered laser light, (2) yield the highest signal-to-noise ratio in the LIF signal, and (3) ensure the reliable and reproducible performance of all components of the experiment. In a first step, we measured the $N_2^+\ B\ ^2\Sigma_u^+ \rightarrow X\ ^2\Sigma_g^+$ fluorescence produced directly by the continuous electron beam on N_2 as a function of electron energy up to 200 eV without the laser beam being present in order to demonstrate the proper performance of the crossed electron-beam–gas-beam arrangement. With the laser beam present, it was found necessary to introduce a delay of about 30–35 ns after the laser pulse had traversed the interaction region before the signal could be recorded in order to ensure that the scattered laser light reaching the PMT had decayed to a level where it no longer swamped the fluorescence signal.

The wavelength control unit of the dye laser served as the master trigger for the timing sequence of the data acquisition procedure. Once the dye laser was positioned at a predetermined starting wavelength, the wavelength control unit triggered the excimer laser. A

small portion of the dye laser output was directed onto a fast photodiode whose output served as the trigger for the gated photon counter. After the laser beam had traversed the interaction region and the abovementioned 30–35 ns delay due to the presence of scattered laser light had elapsed, a first gate (gate A) was opened for 300 ns (which corresponds to about 5 times the radiative lifetime of the N_2^+ B state). The data in gate A contain the LIF signal, any residual background and/or noise, and in case of a continuous electron beam also the N_2^+ $B\ ^2\Sigma_u^+ \rightarrow X\ ^2\Sigma_g^+$ fluorescence produced by the continuous electron beam. After 300 ns, this gate was closed and a second gate (gate B) was opened for the same period of 300 ns. Since after a period of 5 lifetimes any residual LIF signal is negligible, the data in gate B contain only the residual background/noise and again in case of a continuous electron beam also the N_2^+ $B\ ^2\Sigma_u^+ \rightarrow X\ ^2\Sigma_g^+$ fluorescence produced by the continuous electron beam. The LIF signal was then obtained as the difference between the accumulated counts in gate A and gate B. Data at a given wavelength of the laser were typically accumulated for several hundred laser pulses before the wavelength control unit of the dye laser advanced the wavelength of the dye laser by a predetermined increment and the data acquisition cycle was started again. By scanning the laser across the wavelength region of the rotational lines of the N_2^+ $B\ ^2\Sigma_u^+ \rightarrow X\ ^2\Sigma_g^+$ (0,0) vibrational band around 391 nm and detecting the (0,1) band of the same transition at 428 nm one obtains a rotationally resolved LIF spectrum of the (0,0) band in this fashion.

4. Results and discussion

Fig. 2 shows our measured photoemission cross section of the N_2^+ $B\ ^2\Sigma_u^+ \rightarrow X\ ^2\Sigma_g^+$ (0,1) vibrational transition at 428 nm following ionization excitation of ground-state N_2 by electron impact from threshold to 200 eV (no laser beam present). Our relative cross section was normalized to the well-known cross section shape of Borst and Zipf [38] at 120 eV. We note the overall excellent agreement between the two

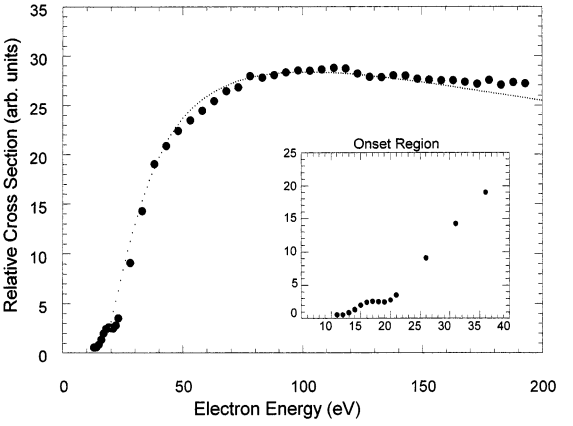

Fig. 2. Photoemission cross section of the N_2^+ $B\ ^2\Sigma_u^+ \rightarrow X\ ^2\Sigma_g^+$ (0,1) vibrational transition at 428 nm following ionization-excitation of ground-state N_2 by electron impact from threshold to 200 eV normalized to the cross section shape of Borst and Zipf [38] at 120 eV. The structure in the near-threshold region is due to the weak (1,5) vibrational band of the N_2 $C\ ^3\Pi_u \rightarrow B\ ^3\Pi_g$ transition following electron-impact excitation of ground-state N_2 which emits at 427 nm and cannot be separated from the N_2^+ fluorescence by our interference filter which has a 10 nm band width. The insert clearly shows the two contributions from the two emission cross sections in the near-threshold region. See text for further details.

cross section curves over the entire energy range, which indicates that our interaction volume remains constant to better than 4% as the impact energy is varied. The structure in our cross section in the near-threshold region is due to the weak (1,5) vibrational band of the N_2 $C\ ^3\Pi_u \rightarrow B\ ^3\Pi_g$ transition following electron-impact excitation of ground-state N_2 which emits at 427 nm and cannot be separated from the N_2^+ fluorescence at 428 nm by our interference filter which has a 10 nm band width. The enlargement in Fig. 2 clearly shows the two contributions from the two emission cross sections in the near-threshold region. The N_2 emission with a threshold near 11 eV shows the typical energy dependence of a spin-forbidden excitation process, a rapid increase above threshold to a maximum in the cross section within a few electron volts above threshold followed by a steep decline toward higher impact energies. The steep decline in the N_2 cross section toward higher impact energies is masked by the onset of the much larger N_2^+ cross section which has a threshold of about 19 eV.

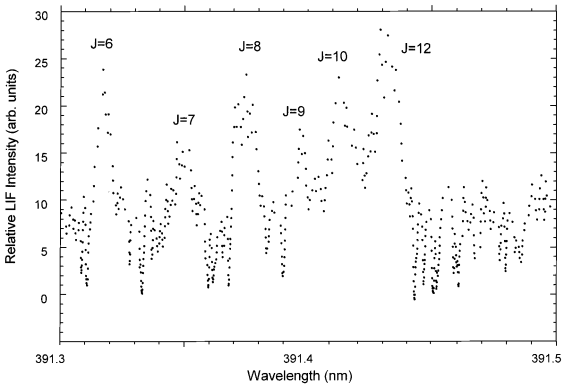

Fig. 3. Rotationally resolved LIF spectrum of the N_2^+ $B\ ^2\Sigma_u^+ \rightarrow X\ ^2\Sigma_g^+$ (0,0) vibrational band near the head of the *P* branch between 391.3 and 391.45 nm obtained at an electron energy of 100 eV. The peaks are labeled by the rotational quantum number *J* of the lower rotational level. Note that the peak labeled $J = 12$ also contains also the $J = 11$, 13–15 rotational lines whose positions lie within ± 0.01 nm of the position of the $J = 12$ line and could not be resolved.

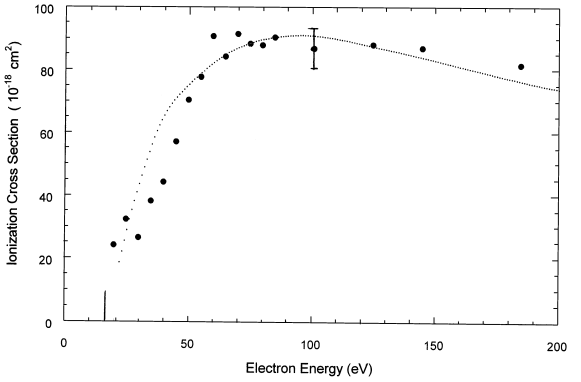

Fig. 4. Absolute N_2^+ (X) ionization cross section in the energy range from threshold (marked by vertical bar) to 200 eV as a function of electron energy. The dotted line is an estimated energy dependence of the N_2^+ (X) cross section normalized to our cross section curve at 75 eV (see text for details). Our absolute cross sections were obtained by normalization of the relative cross section to the absolute cross section value of Doering and Yang [23] at 100 eV. The error bar at 100 eV represents all statistical and systematic errors of our relative cross section, but does not include the 8% uncertainty in the benchmark cross section of Doering and Yang [23].

Fig. 3 shows a part of the rotationally resolved LIF spectrum of the N_2^+ $B\ ^2\Sigma_u^+ \rightarrow X\ ^2\Sigma_g^+$ (0,0) vibrational band near the head of the *P* branch between 391.3 and 391.45 nm obtained at an electron energy of 100 eV. The rotational structure is clearly resolved. The peaks are labeled by the rotational quantum number *J* of the lower rotational level. Note that peak labeled $J = 12$ also contains the rotational lines corresponding to $J = 11$,13–15 whose positions lie within ± 0.01 nm of the position of the $J = 12$ line and could not be resolved. Rotational lines corresponding to *J* values higher than 15 are too weak to appear in the spectrum with appreciable intensity given that the temperature of our gas beam is close to room temperature. We chose the most prominent $J = 12$ peak in the spectrum for the determination of the relative N_2^+ (X) cross section and recorded its LIF intensity for various electron energies. The result is shown in Fig. 4. Also shown in Fig. 4 (dotted line) is an estimated energy dependence of the N_2^+ (X) cross section normalized to our cross section curve at 75 eV. This estimated shape has been obtained by subtracting the N_2^+ *B*-state cross section shape of Borst and Zipf [38] and the N_2^+ *A*-state cross section shape of Piper et al. [39] from the total N_2^+ parent ionization cross section shape of Krishnakumar and Srivastava [29]. As one can see, our measured N_2^+ (X) cross section shape is in good agreement with the estimated shape in the energy region from threshold to 200 eV. The relative cross section curve was put on an absolute scale by normalization to the absolute cross section value of Doering and Yang [23] at 100 eV. We note that if we use the absolute cross sections given in [29,38,39] in order to obtain an estimated absolute N_2^+ (X) cross section, this cross section would lie about 25% below the dotted line shown in Fig. 4. A typical error bar for our cross section is given for the data point at 100 eV. We summed in quadrature the various systematic uncertainties ($< 5\%$ pulse-to-pulse reproducibility of the laser pulse energy, $< 1\%$ stability of each the electron beam current and the gas beam density, $< 4\%$ constancy of the interaction volume as a function of electron energy) and added to it linearly the $< 3\%$ uncertainty in the counting statistics. Not included in the error bar is the 8% uncertainty in the benchmark cross section value of Doering and Yang [23].

Acknowledgements

The authors wish to acknowledge financial support of this work from the U.S. National Science Foundation and from the U.S. National Aeronautics and Space Administration. They also acknowledge helpful discussions with many colleagues during the course of this work, particularly with J.W. McConkey, V. Tarnovsky, and P. Kurunczi.

References

[1] T.D. Märk, G.H. Dunn (Eds.), Electron Impact Ionization, Springer Verlag, Vienna, 1985.
[2] R.K. Janev (Ed.), Atomic and Molecular Processes in Fusion Edge Plasmas, Plenum, New York, 1995.
[3] V. Tarnovsky, K. Becker, Plasma Sources Sci. Technol. 4 (1995) 307.
[4] V. Tarnovsky, K. Becker, Invited Papers, XVIII. ICPEAC, AIP Conference Proceedings No. 295, T. Andersen, B. Fastrup, F. Folkmann, H. Knudsen, N. Andersen (Eds.), AIP, New York, 1994, pp. 234–248.
[5] S.M. Younger, Quantum Theoretical Methods for Calculating Ionization Cross Sections, in Electron Impact Ionization, T.D. Märk, G.H. Dunn (Eds.), Springer Verlag, Vienna, 1985.
[6] S.M. Younger, T.D. Märk, Semi-empirical and Semi-classical Approximations for Electron Ionization, in Electron Impact Ionization, T.D. Märk, G.H. Dunn (Eds.), Springer Verlag, Vienna, 1985.
[7] J.E. Ötvos, D.P. Stevenson, J. Am. Chem. Soc. 78 (1956) 546.
[8] W.L. Fitch, A.D. Sauter, Anal. Chem. 55 (1983) 832.
[9] H. Deutsch, M. Schmidt, Beitr. Plasmaphys. 24 (1984) 475.
[10] H. Deutsch, K. Becker, T.D. Märk, Int. J. Mass Spectrom. Ion Processes 167/168 (1997) 503.
[11] H. Deutsch, K. Becker, R. Basner, M. Schmidt, T.D. Märk, J. Phys. Chem., in press.
[12] D. Margreiter, H. Deutsch, M. Schmidt, T.D. Märk, Int. J. Mass Spectrom. Ion Processes 157 (1990) 100.
[13] H. Deutsch, C. Cornelissen, L. Cespiva, V. Bonacic-Koutecky, D. Margreiter, T.D. Märk, Int. J. Mass Spectrom. Ion Processes 43 (1993) 129.
[14] H. Deutsch, T.D. Märk, V. Tarnovsky, K. Becker, C. Cornelissen, L. Cespiva, V. Bonacic-Koutecky, Int. J. Mass Spectrom. Ion Processes 77 (1994) 137.
[15] D.K. Jain, S.P. Khare, J. Phys. B 9 (1976) 1429; S.P. Khare, W.J. Meath, ibid. 20 (1987) 2101.
[16] M. Bobeldijk, W.J. van der Zande, P.G. Kistemaker, Chem. Phys. 179 (1994) 125.
[17] C.G. Aitken, D.A. Blunt, P.W. Harland, J. Chem. Phys. 101 (1994) 11074; Int. J. Mass Spectrom. Ion Processes 149/150 (1995) 279; C. Vallance, P.W. Harland, R.G.A.R. Maclagan, J. Phys. Chem. 100 (1996) 15021.
[18] Y.-K. Kim, M.E. Rudd, Phys. Rev. A 50 (1994) 3954.
[19] W. Hwang, Y.-K. Kim, M.E. Rudd, J. Chem. Phys. 104 (1996) 2956.
[20] Y.-K. Kim, W. Hwang, N.M. Weinberger, M.A. Ali, M.E. Rudd, J. Chem. Phys. 106 (1997) 1026.
[21] B. Van Zyl, W. Pendleton Jr., J. Geophys. Res. 100 (1995) 23755.
[22] J.P. Doering, J. Yang, J. Geophys. Res. 101 (1996) 19723.
[23] J.P. Doering, J. Yang, J. Geophys. Res. 102 (1996) 9683, 9691.
[24] J.P. Doering, J. Yang, Phys. Rev. A 54 (1996) 3977.
[25] A. Zecca, G.P. Karwasz, R.S. Brusa, Riv. Nuovo Cim. 3 (1996) 1.
[26] D. Rapp, P. Englander-Golden, J. Chem. Phys. 43 (1965) 1464.
[27] Y. Itikawa, M. Hayashi, A. Ichimura, K. Onda, K. Sakimoto, K. Takanayagi, H. Nakamura, T. Takanayagi, J. Phys. Chem. Ref. Data 15 (1986) 985.
[28] R.S. Freund, R.C. Wetzel, R.J. Shul, Phys. Rev. A 41 (1990) 5861.
[29] E. Krishnakumar, S.K. Srivastava, J. Phys. B 23 (1990) 1893.
[30] H.C. Straub, P. Renault, B.G. Lindsay, K.A. Smith, R.F. Stebbings, Phys. Rev. A 54 (1996) 2146.
[31] R.F. Holland, W.B. Meier, J. Chem. Phys. 56 (1972) 5229.
[32] J.R. Peterson, T.J. Moseley, J. Chem. Phys. 58 (1973) 172.
[33] P.W. Zetner, M. Darrach, P. Hammond, W.B. Westerveld, R.L. McConkey, J.W. McConkey, Chem. Phys. 124 (1988) 453.
[34] K.E. Martus, K. Becker, J. Phys. B 22 (1989) L497; K. Martus, S.-H. Zheng, K. Becker, Phys. Rev. A 44 (1991) 1682.
[35] R.B. Siegel, Ph.D. Thesis, City University of New York, 1996.
[36] J.A. Giordmane, T.C. Wang, J. Appl. Phys. 31 (1960) 463.
[37] L. Hüwel, D.R. Guyer, G.-M. Lin, S.R. Leone, J. Chem. Phys. 81 (1984) 3520.
[38] W.L. Borst, E.C. Zipf, Phys. Rev. A 1 (1970) 834.
[39] L.G. Piper, B.D. Green, W.A.M. Blumberg, S. Wolnik, J. Phys. B 19 (1986) 3327.